

## THE QUIESCENT CORE OF TURBULENT CHANNEL FLOW UNDER THE INFLUENCE OF INLET TURBULENCE

**Masoud Asadi**

Department of Energy and Process Engineering  
Norwegian University of Science and Technology  
Trondheim, Norway  
masoud.asadi@ntnu.no

**Md Kamruzzaman**

Department of Energy and Process Engineering  
Norwegian University of Science and Technology  
Trondheim, Norway  
md.kamruzzaman@ntnu.no

**R. Jason Hearst**

Department of Energy and Process Engineering  
Norwegian University of Science and Technology  
Trondheim, Norway  
jason.hearst@ntnu.no

### ABSTRACT

The quiescent core of turbulent channel flow is examined under the influence of inlet turbulence using planar particle image velocimetry. Four cases are tested with matched centerline mean velocities, while the centerline turbulence ranged from 3.7% for the reference case, up to 6.4% for the most turbulent case. A matched friction Reynolds number of  $Re_\tau \approx 770$  is found for all cases, which contrasts with similar measurements in a zero-pressure-gradient boundary layer where  $Re_\tau$  varies with freestream turbulence. The added turbulence increases the frequency of core discontinuity inside the channel and gives rise to new core types. The new cores differ from the conventional ones in their characteristic velocity, while their occurrence increases with turbulence intensity. They are associated with a bulk of low- or high-momentum fluid passing through the measurement domain. Their presence in the channel implies a more turbulent state of the flow inside the core region. It is also observed that, under the effect of increased inlet turbulence intensities, the core boundary moves closer to the wall, which yields thicker cores.

### INTRODUCTION

The so-called quiescent core (QC) of turbulent channel flow was first identified by Kwon *et al.* (2014) as the uniform momentum zone (UMZ) occupying the central region of the channel. It was referred to as ‘quiescent’ because the fluctuations of the streamwise velocity remain low throughout the core. Examining the accumulated probability density function (PDF) of modal velocities (the peaks in the histogram of instantaneous streamwise velocity fields), Kwon *et al.* (2014) stated that the core boundaries could be identified using a constant velocity threshold equal to 95 % of centerline mean velocity (the same constant boundary threshold value was found in later studies by Yang *et al.* (2016, 2019); Jie *et al.* (2019, 2021)). The QC was always present in the flow fields; however, it became discontinuous in some instances. Kwon *et al.* (2014) also observed a sharp jump in the streamwise velocity across the QC boundary which indicated the presence of a shear layer. Yang *et al.* (2016), using direct numerical sim-

ulations, examined the structural organization of the QC by exploring the vortical structures in the flow, stating that the core boundary is surrounded by a vortex pair with the prograde vortex to be the main contributor to the mean shear. Later, Jie *et al.* (2019) examined the effect of the QC on the motion of spheroidal particles in a channel, finding that the motion of the particles also tends to be quiescent in the QC. Following their previous study, Jie *et al.* (2021) assessed the distributions of inertial particles in a turbulent channel flow, stating that particles tend to congregate within the QC.

The sensitivity of zero-pressure-gradient turbulent boundary layers (ZPG-TBL) to the freestream turbulence (FST) above it has been tested extensively (Sharp *et al.*, 2009; Dogan *et al.*, 2016, 2019; Jooss *et al.*, 2021; Hearst *et al.*, 2021). FST is known to suppress the wake region of the velocity profile and increase the friction Reynolds number ( $Re_\tau$ ) of ZPG-TBLs (Sharp *et al.*, 2009; Dogan *et al.*, 2016). It also affects ZPG-TBLs by amplifying normal Reynolds stresses as well as the Reynolds shear stress. Recently, Hearst *et al.* (2021) investigated UMZs of a ZPG-TBL under the effect of FST, stating that increased FST pushes the top boundary of the outermost UMZ towards the wall and increases the velocity jump across this boundary.

Most previous internal flow investigations have primarily focused on Reynolds number effects, e.g., Ng *et al.* (2011); Lee & Moser (2015), and recently, a number of studies have been conducted to investigate wall motions in turbulent channel flow, e.g., Józsa *et al.* (2019); however, the effects of inlet turbulence have not been investigated in great detail for internal flows. Recently, Tuna *et al.* (2019) explored the evolution of flow in a duct with an aspect ratio of 2:1 using different passive grids at the inlet and found that the shear layers met earlier for increasing centerline turbulence intensity. However, the corners certainly affect the flow in the center of a 2:1 duct (Vinueza *et al.*, 2018). Accordingly, to investigate the impacts of added turbulence on the quiescent core of turbulent channel flow, four different turbulence intensities were produced at the inlet of a turbulent channel flow, and PIV measurements were performed in a region far from the inlet.

Table 1. Parameters of the test cases.

Case	Symbol	Color	$u'_0/U_0$ (%)	$U_\tau$ (ms <sup>-1</sup> )
REF	▶	green	3.7	0.460
A	■	magenta	4.8	0.470
B	●	blue	4.9	0.468
C	◆	red	6.4	0.466

## EXPERIMENTAL DETAILS

Experiments were conducted in the air channel flow facility at the Norwegian University of Science and Technology. A centrifugal fan was used to generate the air flow, which blows air through a series of 4 screens through an expansion. The flow then passes through a honeycomb before another screen and then a 48:1 contraction at the end of which is a 600 mm × 50 mm rectangular duct with an aspect ratio of 12:1. An active grid is located 125 mm ( $2.5H$ , where  $H = 2h = 50$  mm is the channel height) downstream of the contraction, followed by a sandpaper trip another 50 mm ( $1H$ ) downstream. The active grid comprises a  $12 \times 2$  array of space-filling 3D-printed PLA plastic rectangular wings, where each wing is attached to a stepper motor. Each stepper motor receives prescribed random rotational direction, velocity, and duration signals. Four test cases were tested, i.e., the reference case ‘REF’ where the active grid was left in its fully open position, thus acting as an additional flow straightener, together with three different active sequences referred to as cases ‘A’, ‘B’, and ‘C’, with increasing centerline turbulence intensity ( $u'_0/U_0$ ). The centerline mean velocity was held constant to within 1% at  $U_0 = 10$  m/s, resulting in a Reynolds number of  $Re_H = U_0 H / \nu = 33,200$ . Further details are given in Table 1. The pressure drop along the channel was measured at 16 pressure taps using a Scanivalve MPS4264 miniature pressure scanner with an accuracy of  $\pm 2\%$  of the full scale. The first tap was located  $7.5H$  downstream of the inlet, and the taps were separated in intervals of 325 mm ( $6.5H$ ). From the pressure drop measurements, the wall shear stress  $\tau$  could be estimated, and from it, the friction velocity  $U_\tau$ . Even though previous studies have observed an increase in friction velocity for a ZPG-TBL subjected to FST (Sharp *et al.*, 2009; Dogan *et al.*, 2016), the friction velocity, listed in table 1, is roughly constant for different cases resulting in an approximately matched friction Reynolds number of  $Re_\tau \approx 770$ .

Planar particle image velocimetry (PIV) measurements were performed in the streamwise—wall-normal plane in the center of the channel  $87H$  downstream of the inlet. Double-frame images (5100 image pairs for each test case) were acquired using a LaVision Imager sCMOS camera (5 megapixel) fitted with a Zeiss Milvus 2/100M lens. The final field-of-view (FOV) was approximately 50 mm × 44 mm, i.e.,  $2h$  in height and  $1.75h$  in length. An industrial smoke machine was utilized to produce particles with a diameter of approximately 1  $\mu$ m, which were injected into the flow at the fan entrance. FOV was illuminated by a Litron Nano PIV laser (Nd-YAG, 532 nm, 200 mJ per pulse). The laser beam was turned into a thin sheet using LaVision light sheet optics. The lens  $f$ -number was set to 11, resulting in a particle size of approximately 2-3 pixels, which helped circumvent pixel-locking issues. A LaVision PTU X synchronized the laser and camera, and the independent samples were recorded at a frequency of

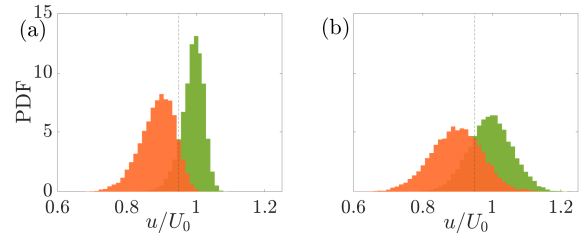


Figure 1. PDFs of the highest (green) and second highest (orange) modal velocities, found in all PIV fields for cases (a) REF, and (b) C. The grey dashed lines mark  $u = 0.95U_0$ . Adapted from Asadi *et al.* (2022).

15 Hz using LaVision DaVis 10.1. The same software was used to process the images using iterative cross-correlation with a final-pass-window size of 48 pixels × 48 pixels with an overlap of 75 %.

## CORE IDENTIFICATION PROCEDURE

The conventional method introduced by Kwon *et al.* (2014) is modified here to identify the QC boundary threshold value with less ambiguity. Since the QC is the UMZ with the highest momentum level in the core, its characteristic velocity corresponds to the highest modal peak in the instantaneous histogram of the velocity fields. Thus, instead of assessing the accumulative PDF of all modal velocities detected in the histograms of instantaneous PIV fields, PDFs of the first and second highest modal velocities are assessed here as the characteristic velocities of the two most robust UMZs of the channel. Figure 1(a) shows these PDFs plotted on top of each other for case REF. A distinguishable trough is exposed between the PDFs, whose corresponding value can be picked as the boundary threshold to identify QCs. Accordingly, a constant boundary threshold value of  $u_{th} = 0.95 U_0$  is chosen. Although the same boundary threshold value is found for the added turbulence cases (A, B, and C), the prominence of the trough diminishes for increased inlet turbulence intensities (e.g., see figure 1(b) for PDFs of case C) due to more spread distributions of the modal peaks. Figure 2 shows three examples of the identified cores in different fields of case C. Figure 2(a) and 2(b) demonstrate a continuous and a discontinuous core of the turbulent channel flow, respectively. These two core types were previously observed by Kwon *et al.* (2014). It is observed here that the discontinuous core events increase in frequency for increased centerline turbulence intensities. In contrast to the results of Kwon *et al.* (2014), the present results include instances in which the QC is not detectable using the opted constant threshold value, particularly for the highly turbulent case C (e.g., figure 2(c)). These instances only occur for the added turbulence cases, and their frequency scales with  $u'_0/U_0$ .

In search of finding the core structure for these fields, in which the conventional QC was not identifiable, the same PDF analysis was repeated. Figure 3(a) represents the resulting PDFs, where a distinct valley is revealed at  $u_{th} = 0.85U_0$ . Also, the PDFs of both the first and second highest peaks are displaced towards lower velocity values while showing the same normal distribution as observed previously in figure 1. This indicates that the core structure is present in these velocity fields; however, a lower threshold value should be utilized to identify them. The lower characteristic velocity of these cores demonstrates a lower momentum level inside the core region compared to the conventional QCs (CQC). Therefore, these new core types are referred to herein as low momentum

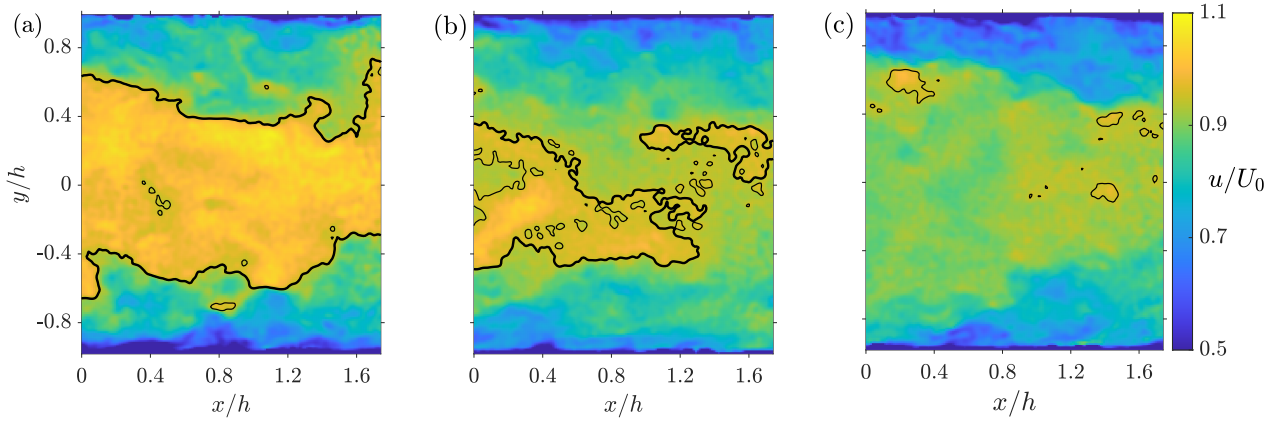


Figure 2. Instantaneous streamwise velocity contours from PIV snapshots of Case C. Contour lines of  $u_{th} = 0.95 U_0$  are indicated with black lines. The thicker lines highlight the QC boundaries. (a) conventional QC, (b) discontinuous QC, and (c) without QC. Adapted from Asadi *et al.* (2022).

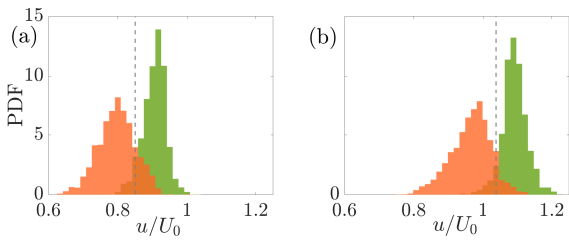


Figure 3. PDFs of the highest (green) and the second highest (orange) modal velocity, found in the PIV fields of (a) instances without QC, and (b) instances identified by presumed threshold value, for case C. The grey dashed line marks  $u = 0.85U_0$  and  $u = 1.04U_0$  in (a) and (b), respectively. Adapted from Asadi *et al.* (2022).

cores (LMC). Furthermore, some of the velocity fields were identified in which a new core type is found inside the traditional QC with a higher boundary velocity threshold. To identify these fields, a higher velocity threshold value ( $1.065U_0$ ) was presumed so that the number of continuous cores identified by this new threshold was close to the number of the previously identified LMCs. Figure 3(b) shows the resulting PDFs of these newly identified fields, indicating an actual boundary threshold value of  $u_{th} = 1.04U_0$ . This new threshold value can be utilized to identify the core structure of these fields. In contrast to LMCs, the PDF of the highest modal peak indicates a higher characteristic velocity for these new cores than that for CQCs. Thus, these new cores take on higher momentum levels and are referred to herein as high momentum cores (HMC). Figure 4(b) represents an example of these fields with the actual core demarcated by the contour lines of  $u_{th} = 1.04U_0$ , demonstrating that the newly identified core was previously hidden within the boundaries of the CQC identified by the constant threshold value of  $0.95U_0$ . The number of the different core types identified in the PIV fields of the different test cases is listed in table 2. Like LMCs, HMCs exist only for the added turbulence cases and occur with the same frequency as LMCs. The occurrence frequency of the new cores, i.e., LMC and HMC, as well as the discontinuous core, increases with increasing centerline turbulence intensity. Nonetheless, the growth rate of the presence of the new core types is greater than that of the discontinuous cores.

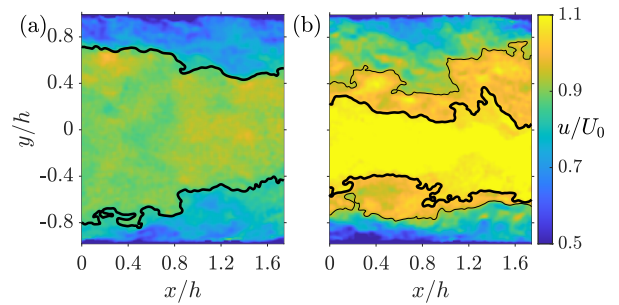


Figure 4. Examples of new core types. (a) an example of a velocity field with a low momentum core (the same field as shown in figure 2(c)), where the core boundaries are marked by the black contour lines of  $u_{th} = 0.85U_0$ . (b) an example of a velocity field with a high momentum core, where the new core boundaries are demarcated by the contour lines of  $u_{th} = 1.04U_0$  (black thick lines) and are located within the previously found conventional QC boundaries marked by the contour lines of  $u = 0.95U$  (black thin lines). Adapted from Asadi *et al.* (2022).

## CORE STATISTICAL ANALYSIS

Parameters of the core location ( $y_l$ ,  $y_u$ , and  $y_c$  denote the core's lower boundary, upper boundary, and center location, respectively, and  $t_c$  is the core thickness) are illustrated in figure 5. For the statistical analysis of these parameters, the core boundaries must be single-valued functions of the streamwise coordinate ( $x$ ). This is not always the case since the core boundaries are usually folded back and forth. Kwon *et al.* (2014) employed the inner-enveloping method to remedy this problem. The same technique is used here, where the closest point to the center of the channel is picked whenever the core boundary does not have a single value at a specified  $x$ . The examples of inner-enveloped core boundaries are shown in figure 5 as well.

Distributions of the core location parameters are represented in figure 6. Figure 6(a) shows the PDF of the core's lower boundary location for the different test cases, where the probability of the presence of the core boundary in the inner regions ( $-0.9 < y_l/h < -0.5$ ) is increased by increasing inlet turbulence intensity. This indicates that increased turbulence pushes the core boundary towards the wall, which is similar to the observation of Hearst *et al.* (2021) that in a ZPG-TBL

Table 2. The presence of the various core types in the PIV fields of each test case as a percentage of total fields (5100).

Core type	Symbol	Color	No. of different core types (%) for case			
			REF	A	B	C
LMC	▲	orange	0	2.3	2.6	11.0
CQC	★	black	97.0	86.6	85.8	68.2
HMC	▼	violet	0	3.2	3.4	11.4
Discontinuous	-	-	3.0	7.9	8.4	9.4

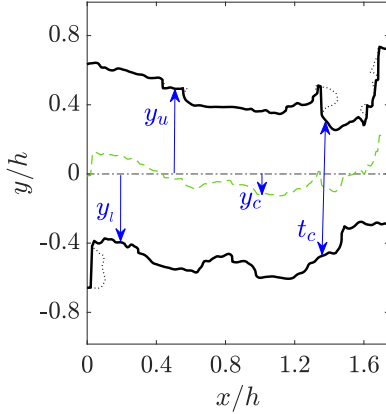


Figure 5. Core location parameters together with enveloped (black solid line) and un-enveloped (black dotted line) core boundaries. The green dashed line shows the core's center position. Adapted from Asadi *et al.* (2022).

subjected to FST, the upper boundary of the outermost UMZ is moved closer to the wall. Figure 6(a) also indicates that the probability of the events where the core's lower boundary is present in the near-wall region ( $y_l/h < -0.9$ ) or is thoroughly dragged above the channel's centerline ( $y_l/h > 0$ ) is equally low for all the test cases. Figure 6(b) illustrates the distribution of the core's center location, where all the PDFs show a normal distribution centered about the channel centerline, as is expected due to the symmetry of the channel. Figure 6(c) shows the PDFs of core thickness, demonstrating that the increased inlet turbulence intensity yields, on average, thicker cores.

Two averaging techniques are utilized to assess the impact of the inlet turbulence on the flow characteristics inside and outside the core region. The first technique zonally averages the streamwise velocity and its fluctuations (inner normalized) when the flow is situated inside and outside the core region, which are denoted by subscripts 'i' and 'o', respectively (see Kwon *et al.*, 2014, section 4 for details). As shown in figure 7(a), the zonally averaged streamwise velocity takes on an approximately constant value inside the core region which scales with  $U_0$ . The profiles collapse for all the cases inside the core region, indicating the same mean velocity inside the core for different test cases irrespective of the presence of the new core types. The profiles also match outside the core region. On the other hand, figure 7(b) demonstrates zonally averaged streamwise fluctuation profiles inner normalized by  $U_0^2$ , indicating an increase in turbulent fluctuations inside the core with increasing  $u'_0/U_0$ . This happens due to the presence of

the new core states with different characteristic velocities than CQCs'. The same behavior is also noticed for the zonally averaged streamwise velocity fluctuations outside the core region.

The other averaging method is called conditional averaging. In this method, the wall-normal coordinate ( $y$ ) is translated to the core lower boundary ( $y_l$ ), and the streamwise velocity and its fluctuations are averaged across the core boundary (denoted by  $\langle \rangle$ ). Due to the presence of the new core states with different boundary threshold values, the instantaneous streamwise velocities were offset by the local  $u_{lh}$  before averaging to make the profiles comparable for different test cases. Figure 7(c) shows the conditionally averaged streamwise velocity profiles suggesting that the added turbulence does not affect the behavior of the velocity profile near the boundary of the core as a sharp jump is observed in the vicinity of the core boundary for all the test cases. This is typical of UMZs and indicative of the thin shear layer which forms the boundary of the core (Kwon *et al.*, 2014; Yang *et al.*, 2016). Furthermore, an almost constant velocity is observed inside the core away from the boundary, as was expected for UMZs. Nevertheless, the fitted lines suggest that the added turbulence increases the velocity jump across the core boundary, which is in line with the observation made by Hearst *et al.* (2021) regarding the increased velocity jump across the upper-most UMZ of a ZPG-TBL under the influence of FST. This can be explained by recalling the trend observed in figure 6(a), where the core's lower boundary is located closer to the wall under the effect of inlet turbulence. Therefore, under the influence of increased inlet turbulence, the core is closer to the inner regions with lower streamwise velocity values, which increases the velocity jump across the core boundary. Figure 7(d) demonstrates conditionally averaged streamwise fluctuations. The order of the profiles outside the core boundary scales with  $u'_0/U_0$  and indicates an increasing trend for increased centerline turbulence intensities. Meanwhile, a low turbulence level is observed inside the core region, approximately equal for the different cases regardless of the added turbulence intensity. This may seem to contrast with the trends observed in figure 7(b). However, the key to this implausible paradox lies in the difference between the two averaging schemes. The zonal-averaging analysis assesses the fluctuations of the streamwise velocity relative to the zonally averaged velocity in different locations within the channel, where the emergence of the new cores with different characteristic velocities affects the zonally averaged fluctuations level inside the core region (the results are presented in the following section). At the same time, the conditional-averaging scheme assesses the fluctuations of the streamwise velocity offsetting the velocities by the local boundary threshold value; thereby, the region inside the core appear to be quiescent regardless of the core momentum level.

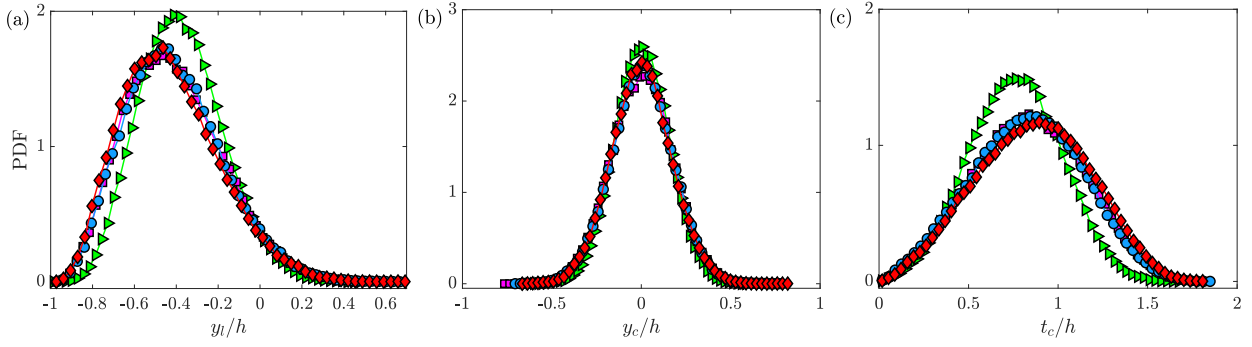


Figure 6. PDF of (a) the core's lower boundary location, (b) the core's center location, and (c) the core thickness, for different test cases. See table 1 for symbols and colors. Adapted from Asadi *et al.* (2022).

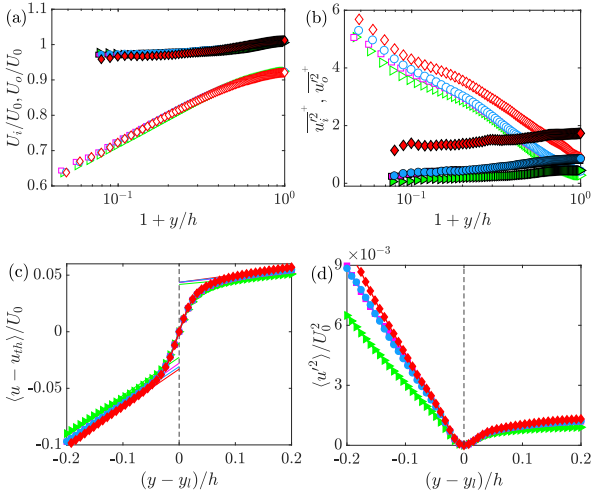


Figure 7. Zonally averaged profiles of streamwise (a) velocity and (b) turbulent fluctuations, inside the core (filled symbols) and outside of it (open symbols) for the different test cases. Conditionally averaged profiles of streamwise (c) velocity and (d) turbulent fluctuations across the core boundary for the different test cases (the grey dashed line shows the core boundary). See table 1 for symbols and colors. Adapted from Asadi *et al.* (2022).

## STATISTICAL ANALYSIS OF NEW CORES

In order to further explore the characteristics of the newly identified core types, the statistical analysis performed in the previous section is repeated here for the different continuous core types. Since case C has the highest number of the newly identified cores, different continuous core types of this test case are analyzed here as an example. The discontinuous cores are discarded in the analysis of this section.

Similar to figure 6, figure 8 illustrates the distributions of core's location parameters for the different core types of case C. PDFs of the core's lower boundary location are shown in figure 8(a), where the lower boundary of LMCs appears to be located closer to the wall compared with CQCs'. Conversely, the lower boundary of HMCs generally resides closer to the channel centerline than that of CQCs. Once more, due to the symmetry of the channel, a normal distribution, centered at  $y/h = 0$ , is observed for PDFs of the core's center location regardless of the core type. Considering the location of the cores' lower boundary, this implies thicker LMCs and thinner HMCs on average, as shown in figure 8(c).

Repeating the zonal averaging technique for different

core types of case C, the zonally averaged profiles are presented in figures 9(a) and 9(b). As shown, the flow takes on different constant mean velocity levels when located inside LMCs, CQCs, or HMCs. These constant velocity levels can be considered as the cores' characteristic velocities, which are  $0.9U_0$ ,  $1.0U_0$ , and  $1.1U_0$  for LMCs, CQCs, and HMCs, respectively, indicating different momentum levels of each core type. Nonetheless, LMCs and HMCs almost neutralize each other when cumulatively averaged (figure 7(a)). Figure 9(b) illustrates zonally averaged streamwise fluctuation profiles, demonstrating an equally low level of fluctuations within the different cores. As stated in the previous section, the different velocity levels within the cores indicate a generally more turbulent flow inside the core region for increased inlet turbulence intensities (figure 7(b)). However, when the deviations of the instantaneous velocity from the zonally averaged velocity are assessed for each core type separately, a low level of fluctuations is indicated (figure 9(b)).

Figure 9(c) shows the conditionally averaged streamwise velocity profiles for the different core types, where the profiles are matched both inside and outside of the core region. This indicates that the shape of the velocity profile and the magnitude of the relative velocity jump are independent of the core momentum level. The same concept can be observed in figure 9(d), where a uniformly low level of conditionally averaged streamwise velocity fluctuations is observed inside the core region, verifying that each core is a localized UMZ and that the identification process utilized in this study is reliable.

## CONCLUSIONS

The inlet turbulence effect on the QC of turbulent channel flow was investigated using PIV measurements in a region far from the inlet. Four different inlet turbulence levels were produced using an active grid located at the inlet of the channel. The centerline mean velocities were matched for the different test cases.  $U_\tau$  did not show any correlation with the centerline turbulence intensity as opposed to the previous observations regarding an increase in  $U_\tau$  of a ZPG-TBL with increasing FST intensities (Sharp *et al.*, 2009; Dogan *et al.*, 2016). Furthermore, the results indicate that the inlet turbulence significantly impacts the core of turbulent channel flow. It considerably influences the momentum level of the core and generates new core types with lower and higher momentum levels (LMC and HMC, respectively) than that of the conventional quiescent core (CQC). As a result, different boundary threshold values should be utilized to identify each core type correctly. Inlet turbulence also manipulates the frequency that the core appears in various types. Thereby, the number of LMCs and HMCs, as well as the discontinuous cores, increases with

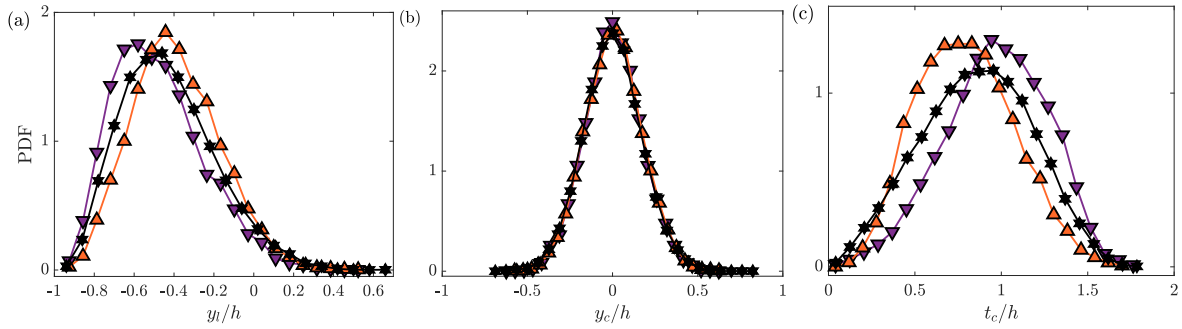


Figure 8. PDF of (a) the core's lower boundary location, (b) the core's center location, and (c) the core thickness, for the different continuous core types of case C. See table 2 for symbols and colors. Adapted from Asadi *et al.* (2022).

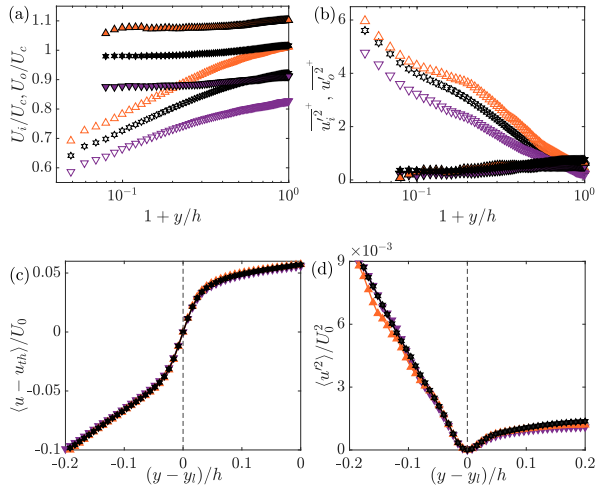


Figure 9. Zonally averaged profiles of streamwise (a) velocity and (b) turbulent fluctuations, inside the core (filled symbols) and outside of it (open symbols) for the different continuous core types of case C. Conditionally averaged profiles of streamwise (c) velocity and (d) turbulent fluctuations across the core boundary the different continuous core types of case C (the grey dashed line shows the core boundary). See table 2 for symbols and colors. Adapted from Asadi *et al.* (2022).

increasing inlet turbulence intensity. The passage of new core types with different momentum levels implies a higher turbulence level of the flow situated within the core. Nevertheless, when each core is observed separately, it possesses a uniform characteristic velocity and a low turbulence intensity within its boundaries as an indication of the common nature of the cores as UMZs.

Although the core possesses different momentum levels, its persistence indicates that it keeps driving the fluid in internal flows, even when the inlet is far from the canonical case.

For more details on this work and greater discussion of the results, see Asadi *et al.* (2022).

## REFERENCES

- Asadi, Masoud, Kamruzzaman, Md & Hearst, R Jason 2022 The effect of inlet turbulence on the quiescent core of turbulent channel flow. *Journal of Fluid Mechanics* **935** (A37).  
Dogan, E., Hanson, R. & Ganapathisubramani, B. 2016 Interactions of large-scale free-stream turbulence with turbulent boundary layers. *J. Fluid Mech.* **802**, 79–107.  
Dogan, Eda, Hearst, R. Jason, Hanson, Ronald E. & Ganapathisubramani, Bharathram 2019 Spatial characteristics of

a zero-pressure-gradient turbulent boundary layer in the presence of free-stream turbulence. *Physical Review Fluids* **4** (8), 084601.

Hearst, R. Jason, de Silva, Charitha M., Dogan, Eda & Ganapathisubramani, Bharathram 2021 Uniform-momentum zones in a turbulent boundary layer subjected to freestream turbulence. *Journal of Fluid Mechanics* **915**, A109.

Jie, Yucheng, Andersson, Helge I. & Zhao, Lihao 2021 Effects of the quiescent core in turbulent channel flow on transport and clustering of inertial particles. *International Journal of Multiphase Flow* **140**, 103627.

Jie, Yucheng, Xu, Chunxiao, Dawson, James R., Andersson, Helge I. & Zhao, Lihao 2019 Influence of the quiescent core on tracer spheroidal particle dynamics in turbulent channel flow. *Journal of Turbulence* **20** (7), 424–438.

Jooss, Yannick, Li, Leon, Bracchi, Tania & Hearst, R. Jason 2021 Spatial development of a turbulent boundary layer subjected to freestream turbulence. *Journal of Fluid Mechanics* **911**, A4.

Józsa, T. I., Balaras, E., Kashtalyan, M., Borthwick, A. G. L. & Viola, I. M. 2019 Active and passive in-plane wall fluctuations in turbulent channel flows. *J. Fluid Mech.* **866**, 689–720.

Kwon, Y.S., Philip, J., de Silva, C.M., Hutchins, N. & Monty, J.P. 2014 The quiescent core of turbulent channel flow. *Journal of Fluid Mechanics* **751**, 228–254.

Lee, M. & Moser, R. D. 2015 Direct numerical simulation of turbulent channel flow up to  $Re_\tau \approx 5200$ . *J. Fluid Mech.* **774**, 395–415.

Ng, H. C. H., Monty, J. P., Hutchins, N., Chong, M. S. & Marusic, I. 2011 Comparison of turbulent channel and pipe flows with varying Reynolds number. *Exp. Fluids* **51**, 1261–1281.

Sharp, N. S., Neuscamman, S. & Warhaft, Z. 2009 Effects of large-scale free stream turbulence on a turbulent boundary layer. *Physics of Fluids* **21** (9), 095105.

Tuna, B. A., Yarusevych, S., Li, X., Ren, Y. & Shi, F. 2019 Investigation of the effect of inlet turbulence and Reynolds number on developing duct flow. *J. Fluids Eng.* **141** (5), 051401.

Vinuesa, Ricardo, Schlatter, Philipp & Nagib, HM 2018 Secondary flow in turbulent ducts with increasing aspect ratio. *Physical Review Fluids* **3** (5), 054606.

Yang, Jongmin, Hwang, Jinyul & Sung, Hyung Jin 2016 Structural organization of the quiescent core region in a turbulent channel flow. *International Journal of Heat and Fluid Flow* **62**, 455–463.

Yang, Jongmin, Hwang, Jinyul & Sung, Hyung Jin 2019 Influence of wall-attached structures on the boundary of the quiescent core region in turbulent pipe flow. *Physical Review Fluids* **4** (11), 114606.